Homogenization of plain weave composites with imperfect microstructure: Part I – Theoretical formulation

Jan Zeman [a,*] Michal Šejnoha [a]

[a] *Department of Structural Mechanics, Faculty of Civil Engineering, Czech Technical University in Prague, Thákurova 7, 166 29, Prague 6, Czech Republic*

Abstract

A simple procedure is presented for the determination of a Periodic Unit Cell (PUC) for plain weave fabric composites with reinforcement imperfections. Geometrical parameters of the PUC are determined so that the resulting PUC resembles the real geometry of a composite, obtained from digitized micrographs of plain weave cross-sections, as close as possible. As the first step, the morphology of a real composite is described by appropriate statistical descriptors. Then, the parameters of the idealized unit cells follow from minimization of the objective function defined as the least square difference of the statistical descriptor related to the original microstructure and to the idealized unit cell, respectively. Once the desired geometrical parameters are determined, the Finite Element model of a woven composite is formulated and used to predict the overall response of the composite by the numerical homogenization method. The quality of the resulting unit cells is addresses from the point of view of effective elastic properties to examine the applicability and limitations of this procedure and to provide modelling strategy for analysis of real world material systems.

Key words: woven composites, periodic unit cell, reinforcement imperfections, microstructural statistics, stochastic optimization, numerical homogenization

1 Introduction

The remarkable material properties offered by composite materials such as high strength, light weight, corrosive resistance and affordability, etc., have

* Corresponding author. Tel.:+420-2-2435-4482; fax:+420-2-2431-0775
Email address: zemanj@cml.fsv.cvut.cz (Jan Zeman).

resulted in their use in diverse high-performance engineering applications. Among the most prominent material systems complying with the aforementioned requirements remain polymer matrix systems reinforced either by aligned fibers, whiskers or fabrics. The popularity of latter materials, in particular, is under continuous rise due to advantageous strength/weight ratio, easiness of manipulation and low production costs.

The complex three-dimensional structure of woven fabric composites, however, makes the analysis and prediction of the overall properties of these material system a relatively difficult task. A number of simplified analytical approaches has been proposed to obtain inexpensive closed-form estimates of the overall behavior of such material systems, starting from modified classical laminate theories approach initiated by Ishikawa and Chou [1,2] for simplified models of geometry and further extended by, e.g., Naik and Shembekar [3]. Alternative methods start from the classical energy principles, see, e.g., Kregers and Malbardis [4] and Pastore and Gowayed [5]. An application of the Mori-Tanaka method to the determination of overall elastic properties of composite was presented by Gommers et al. [6].

In the last decade, the finite element-based methods has been employed for the analysis of woven fabric composites. In theory, the structure of woven composites can be fully described by clearly defined periodic unit cell, which makes asymptotic homogenization techniques rather attractive for the analysis of these materials. The numerical analysis of woven composites originated from the pioneering works of Zhang and Harding [7] for a simplified two-dimensional model and by Paumelle at al. [8,9] for a fully three-dimensional behavior. These studies were further followed and extended by, e.g., Dasgupta and Bhandarkar [10], Chapman and Whitcomb [11] and Whitcomb and Sriregan [12]. For a more detailed discussion, overview and comparison of different methods see, e.g., reviews by Cox and Flanagan [13], Byström et al. [14] and Chung and Tamma [15].

Although all the above analyses rely on the idealized geometry of woven fabric composites, it is well-understood that the collective properties of these materials are to a great extent influenced by imperfections developed during the fabrication process. In this context the waviness, misalignment and/or non-uniform cross-sectional aspect ratio of tows in the longitudinal direction play the main role in assessing the overall behavior of such material systems. In this regard, the formulation of a reliable and accurate numerical model is of paramount importance. Note that simplified models of geometry, which do not account for reinforcement imperfections, are not valid even for carefully prepared laboratory samples, see Fig. 1.

On the experimental level, the effects of woven path imperfections were qualitatively investigated in several works, see, e.g., Breiling and Adams [16],

Fig. 1. An example of textile composite micrograph. Courtesy of B. Košková, Technical University of Liberec

Košek and Košková [17], Košková and Vopička [18], Roy [19] and Yurgartis et al. [20]; the systematic classification and discussion of sources of individual types of imperfection can be found in Pastore [21]. On the analytical level, these issues were incorporated into the framework of laminate theories by Shembekar and Naik [22] who introduced a possible shift of individual layers in their model and in works of Yushanov and Bogdanovich [23,24], who considered a general random imperfections to the tow path and used the stiffness averaging method to obtain statistics on the overall elastic moduli. For the numerical analyses of this phenomenon see the works of Woo and Whitcomb [25] for the three-dimensional geometry of the woven fabric composite and Byström et al. [14,26] for a simplified two-dimensional model where the influence of relative shift of individual layers was carefully investigated.

In the present work, a different strategy is adopted to incorporate, at least to some extent, the reinforcement imperfections into the geometrical model of the unit cell. In particular, we follow the path set in papers by Povirk [27] and by Zeman and Šejnoha [28]. In theses works, the idealized geometrical model of the analyzed composite is defined in terms of a certain periodic unit cell with geometrical parameters derived by matching microstructural statistics of a real microstructure and the searched PUC. For two-dimensional binary microstructures, the efficiency of this approach was numerically demonstrated for composites with elastic [27,28], linearly viscoelastic [29], non-linearly viscoelastic [30] and viscoplastic [31] phases. Moreover, using the model of plain weave geometry proposed by Kuhn and Charalambides [32] in combination with binary images of real composites, this modeling strategy can be extended to the modeling of woven composites in rather straightforward way.

The subject of the present work is closely related to recent papers on the problems of reconstructing random media with specified microstructural functions. In particular, Rintoul and Torquato [33] proposed a method for the reconstruction of particulate systems based on the radial distribution function combined with the Simulated Annealing Method. This work was further extended by Yeong and Torquato [34], where the isotropized lineal path and the two-point probability functions were used in the reconstruction process; the problems of

three-dimensional microstructures reconstruction from two-dimensional cross-sections [35] and real-world materials [36,37] were also considered. The importance of using non-isotropized descriptors was recognized and addressed in [38] and further extended in [39], where the hexagonal grid sampling was advocated. Finally, the recent work of Rozman and Utz [40] revealed that the non-uniqueness problems, reported in previous studies, can be, to a great extent, attributed to artificial isotropy of optimized function and to convergence of the selected optimization method to a local minimum.

The rest of the paper is organized as follows. Section 2 briefly reviews quantification of microstructure morphology and describes the algorithms used for the analysis of the digitized microstructural images. Section 3 then introduces the geometrical model used in the current work, formulates the optimization problem to be solved and presents the used optimization algorithm. Section 4 demonstrates the application of these principles to two-layer composites with misaligned layers and addresses the quality of the unit cell from the point of view of their effective elastic properties to explore the applicability of the presented approach. The paper ends with a brief discussion of the extension and future development of the presented procedure.

In the following text, $\mathbf{a}$, $\boldsymbol{a}$ and $\mathbf{A}$ denote a vector, a symmetric second-order and a fourth-order tensor, respectively. The standard summation notation is adopted, i.e., by $\mathbf{A} : \boldsymbol{b}$ we denote the sum $A_{ijkl}b_{kl}$ while $\boldsymbol{a} \cdot \mathbf{b}$ stands for $a_i b_i$, where the summation with respect to repeated indices is used. The symbol $\{\mathsf{a}\}$ is reserved for a column matrix or a vectorial representation of symmetric second-order tensor while the notation $[\mathsf{L}]$ is employed for a matrix representation of a fourth-order tensor [41,42]. Finally, for all arrays, the C language-style indexing is used, i.e., the first entry on an one-dimensional array a with dimension N is denoted a_0 while the last entry of the array is denoted as a_{N-1}.

2 Microstructure description

This section outlines evaluation of various statistical descriptors, which arise in the analysis of two-phase media with random arrangement of individual phases. With regard to application of these principles to the analysis of two-dimensional sections of plain weave composites we focus on capturing the non-isotropy of the underling microstructure. For a more detailed discussion on quantification of microstructure morphology, see the recent monograph of Torquato [43].

2.1 *n-point probability functions*

To reflect a random character of a heterogeneous medium it is convenient to introduce a sample space $\mathcal{S}$ defined as a collection of samples α with $p(\alpha)$ defining the probability density of α in $\mathcal{S}$. To provide a general description of morphology of such media we consider a characteristic function of the r-th phase $\chi_r(\mathbf{x}, \alpha)$ defined as

$$\chi_r(\mathbf{x}, \alpha) = \begin{cases} 1, \text{ if } \mathbf{x} \in D_r(\alpha), \\ 0, \text{ otherwise}, \end{cases} \tag{1}$$

where $D_r(\alpha)$ denotes the domain occupied by the r-th phase. The n-point probability function $S_{r_1,\ldots,r_n}$ is then given by

$$S_{r_1,\ldots,r_n}(\mathbf{x}_1, \ldots, \mathbf{x}_n) = \int_{\mathcal{S}} \chi_{r1}(\mathbf{x}_1, \alpha) \cdots \chi_{rn}(\mathbf{x}_n, \alpha) p(\alpha) \, \mathrm{d}\alpha. \tag{2}$$

In the following, we limit our attention to functions of the order of one and two, since higher-order functions are quite difficult to determine in practice. Therefore, description of a random medium will be restricted to the information contained in the *one-point probability* function $S_r(\mathbf{x})$ and the *two-point probability* function $S_{rs}(\mathbf{x}_1, \mathbf{x}_2)$, respectively.

Assuming the *statistical homogeneity* of the analyzed medium and validity of the *ergodic hypothesis*, the one and two-point probability functions reduce to [43,44]

$$S_r = c_r, \; S_{rs}(\mathbf{x}) = \frac{1}{|V|} \int_V \chi_r(\mathbf{x}, \alpha) \chi_s(\mathbf{x} + \mathbf{y}, \alpha) \, \mathrm{d}\mathbf{y}, \tag{3}$$

with c_r denoting the volume fraction of the r-th phase and $|V|$ standing for the volume (area) of the analyzed sample.

Various sampling methods can be employed to determine the values of one- and two-point probability functions, starting from simple Monte-Carlo based techniques, later refined by the sampling template approach [45] to sample isotropized values of two-point probability functions. However, in order to avoid well-known problems with using isotropized values in random media reconstruction [39,37,40], the Fourier-transform procedure [46] is employed in the present work to sample the two-point probability function. To this end, we consider a discretization of the microstructure in terms of $W \times H$ bitmap and denote the pixel located in the i-th row and j-th column as $\chi_r(i, j)$. Assuming the microstructure periodicity, Eq. (3) can be replaced by

$$S_r = \frac{1}{WH} \sum_{i=0}^{W-1} \sum_{j=0}^{H-1} \chi_r(i,j), \tag{4}$$

$$S_{rs}(m,n) = \frac{1}{WH} \sum_{i=0}^{W-1} \sum_{j=0}^{H-1} \chi_r(i,j)\chi_s((i+m)\%W, (j+n)\%H), \tag{5}$$

where $a \,\%\, b$ stands for a modulo b. The sum (5) can be then replaced by the Discrete Fourier transform as

$$S_{rs}(m,n) = \frac{1}{WH}\mathrm{IDFT}\{\mathrm{DFT}\{\chi_r(m,n)\}\overline{\mathrm{DFT}\{\chi_s(m,n)\}}\}, \tag{6}$$

where $\bar{\cdot}$ denotes the complex conjugate and $\mathrm{DFT}\{\cdot\}$, $\mathrm{IDFT}\{\cdot\}$ stand for the Discrete Fourier Transform and its inverse, respectively.

Of course, the Fast Fourier Transform, which needs only $O(WH\log(WH) + WH)$ operations compared to the $O(W^2H^2)$ operations needed by Eq. (5), is called to carry out the numerical computation. Moreover, the possibility of using highly optimized software libraries permits to efficiently analyze even high-resolution bitmaps within a reasonable time.

2.2 Lineal path function

As already noted in the previous section, the determination of probability functions of order higher than two encounters serious difficulties, both analytical and numerical. However, these functions still contain important amount of information not correctly captured by low-order probability functions. To overcome this difficulty, one can study low-order microstructural descriptors based on a more complex fundamental function which contains more detailed information about phase connectedness and hence certain information about long-range orders. The lineal path function [47], briefly discussed in this section, is a representative of such indicators.

To maintain formal similarity with the discussion of the n-point probability functions, we first introduce a random function $\lambda_r(\mathbf{x}_1, \mathbf{x}_2, \alpha)$ as

$$\lambda_r(\mathbf{x}_1, \mathbf{x}_2, \alpha) = \begin{cases} 1, \text{ if } \mathbf{x}_1\mathbf{x}_2 \subset D_r(\alpha), \\ 0, \text{ otherwise,} \end{cases} \tag{7}$$

i.e., a function which equals to one when the segment $\mathbf{x}_1\mathbf{x}_2$ is contained in the r-phase for the sample α and equals to zero otherwise. The lineal path function [47], giving the probability that the $\mathbf{x}_1\mathbf{x}_2$ segment is fully contained in

the phase r, then follows directly from the ensemble averaging of this function

$$L_r(\mathbf{x}_1, \mathbf{x}_2) = \int_{\mathcal{S}} \lambda_r(\mathbf{x}_1, \mathbf{x}_2, \alpha) p(\alpha) \, \mathrm{d}\alpha. \tag{8}$$

Under the assumptions of statistical homogeneity, the lineal path function simplifies, in analogy with the two-point probability function, as

$$L_r(\mathbf{x}_1, \mathbf{x}_2) = L_r(\mathbf{x}_1 - \mathbf{x}_2). \tag{9}$$

Similarly to the n-point probability function, an elementary Monte Carlo-based simulation procedure can be used again for the evaluation of lineal path function, i.e., we randomly throw segments into a medium and count the cases when the segment is fully contained in a given phase. Computationally more intensive approach, however, can be employed following the idea of sampling template introduced in [45].

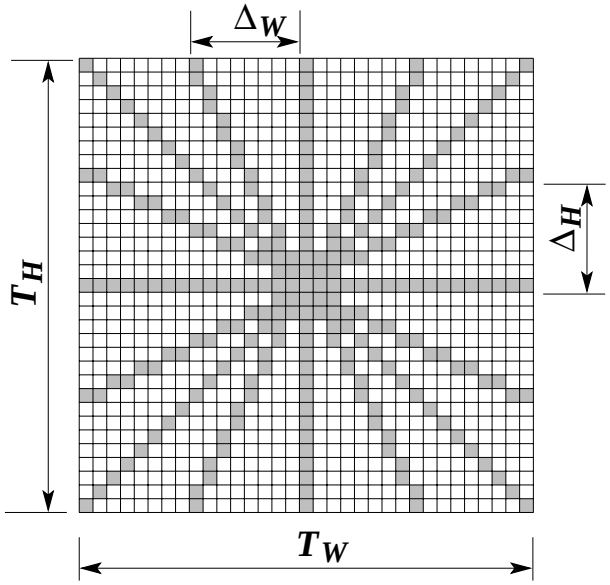

Fig. 2. An example of sampling template

To that end, we form a sampling template with dimensions $T_W \times T_H$ pixels. Then, we draw N_d segments, each of them consisting of $N_\ell(i)$ pixels, from the center of a template to the points on the template boundary separated by given discrete steps Δ_W and Δ_H (see Figure 2). Sampling the values of the the lineal path function for given direction and phase starts from placing the template center at a given point found in the phase r and then marking the pixel at which the segment corresponding to the selected direction meets the other phase. Then, counters corresponding to pixels of a given segment which are closer to the center than the marked pixel are increased by one while the remaining ones are left unchanged. The value of the lineal path function can be then obtained either by stochastic sampling (randomly throwing template center in a medium) or deterministic sampling (template center is successively

placed in all pixels of a bitmap) and averaging the obtained results. Moreover, the latter method allows us to actually use only a half of the sampling template, provided that the analyzed microstructure is statistically homogeneous. Note that even though this procedure basically needs only integer-based operations, it is still substantially slower than the FFT-based approach. Hence, a relatively sparse sampling template is unavoidable if one wishes to keep the efficiency of this procedure comparable to the determination of the two-point probability function.

3 Unit cell definition

As suggested in the introductory part, a realistic model of composite geometry is needed in order to obtain reliable estimates of both the local and overall response of real composites under certain loading conditions. However, such a model, to be statistically representative of the composite, might be quite complex leading to an enormous computational cost. The computational feasibility, on the other hand, calls for rather simple models usually specified in terms of small periodic unit cells. The present section attempts to reconcile these competing requirements by formulating a small periodic unit cell, which yet incorporates the knowledge of real composite geometry with various types of reinforcement imperfections.

3.1 Geometrical model

In this contribution, only the irregularities represented by disordered path of the fiber tow are considered. In general, such imperfections can be quantified by taking two-dimensional images of a tow cross-section along its longitudinal axis; i.e. we attempt to approximate three-dimensional microstructure on the basis of two-dimensional data. Although techniques for constructing three dimensional microstructural images have been recently introduced [48–50, and references therein], they are rather laborious and extremely computationally demanding even for elastic materials. Moreover, it was demonstrated in [35,36,51] that, at least for some classes of materials, the data obtained from two-dimensional sections allow reconstructing the three-dimensional microstructural configurations with satisfactory details.

Literature offers a manifold of geometric models for the description of plain weave geometry with varying level of sophistication. In this work, the model of fabric weave composite proposed by Kuhn and Charalambides [32] is used since it is reasonably simple to implement and directly incorporates typical features of real composites reported in [20]. The present model is fully determined by

four parameters a, b, g and h, see Fig. 3. For the sake of completeness, a brief discussion of the geometrical model is included in Appendix A; in this section, we restrict our attention to two-dimensional cross-sections located in the xz plane.

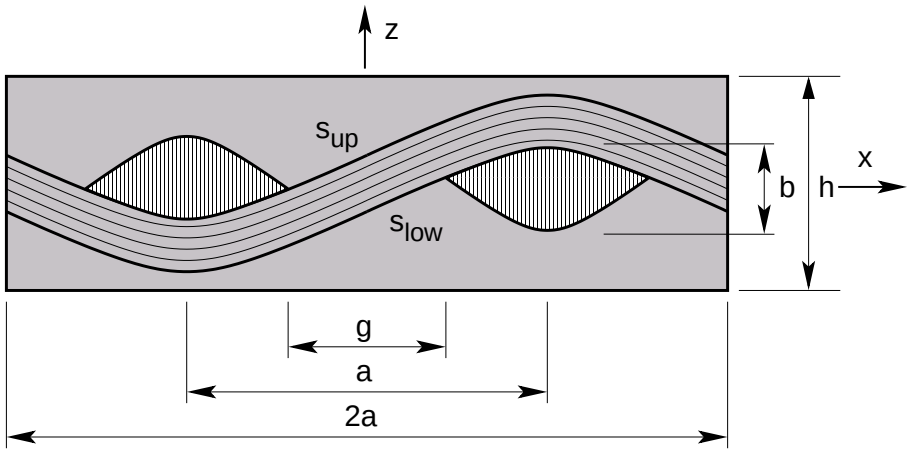

Fig. 3. Geometrical parameters of a plain weave PUC

For the transverse cross-sectional plane located in the middle of the weave, the fill and warp bundle surface functions s_{fill} and s_{warp}, Eq. (A.8), reduce to, see Fig. 3,

$$s_{\text{low}}(x) = \begin{cases} \dfrac{b}{2}\left(\sin\left(\dfrac{\pi x}{a}\right) - \dfrac{x(1-\delta)}{g} - \dfrac{1}{2}(1+\delta)\right) & 0 \le x < \dfrac{g}{2} \\ -\dfrac{b}{2}\left(1 + (1+\beta)\sin\left(\dfrac{\pi(2x-g)}{2(a-g)} - \beta\right)\right) & \dfrac{g}{2} \le x \le \dfrac{a}{2} \end{cases}, \tag{10}$$

$$s_{\text{up}}(x) = \begin{cases} \dfrac{b}{2}\left(\sin\left(\dfrac{\pi x}{a}\right) - \dfrac{x(1-\delta)}{g} + \dfrac{1}{2}(1+\delta)\right) & 0 \le x < \dfrac{g}{2} \\ \dfrac{b}{2}\left(\sin\left(\dfrac{\pi x}{a}\right) + \delta\right) & \dfrac{g}{2} \le x \le \dfrac{a}{2} \end{cases}, \tag{11}$$

where coefficient β is defined in Eq. (A.4) and $\delta = (1+\beta)\cos(\beta)$. Values of function s_{low} and s_{up} for $x > a/2$ and $x < 0$ follow from obvious symmetry of the PUC.

3.2 Objective function

Having chosen the model for the description of the geometry of a PUC, one needs to define a certain objective function, which quantifies the difference between the original microstructure and the idealized periodic unit cell. Following the general procedure discussed in Section 2, the fundamental *bundle*

characteristic function $\chi_f(x,z,\alpha)$ is simply provided by the relation

$$\chi_f(x,z,\alpha) = \begin{cases} 1, \text{ if } s_{\text{low}}(x) \leq z \leq s_{\text{up}}(x) \text{ for sample } \alpha \\ 0, \text{ otherwise.} \end{cases} \tag{12}$$

This characteristic function χ_f can be employed to discretize the PUC cross section into the form of a $W \times H$ bitmap. Then, assuming the periodicity of the microstructure, the two point probability function follows from Eq. (6). Similarly, the matrix lineal path function L_m for a given digitized periodic unit cell can be determined by the sampling template method introduced in Section 2.2.

To determine "statistically" optimal parameters of the periodic unit cell, the parameters a, b, g and h are found by minimizing certain objective functions. Similarly to [34,35,37], objective functions incorporating the two-point matrix probability function S_{mm}, matrix lineal path function L_m or their combination are considered,

$$F_S(\mathbf{x}) = \sum_{i=-i_{\max}}^{i_{\max}} \sum_{j=-j_{\max}}^{j_{\max}} \left(\overline{S}_{mm}(i,j) - S_{mm}(i,j)\right)^2, \tag{13}$$

$$F_L(\mathbf{x}) = \sum_{i=0}^{N_d-1} \sum_{j=0}^{N_\ell(i)-1} \left(\overline{L}_m(i,j) - L_m(i,j)\right)^2, \tag{14}$$

$$F_{S+L}(\mathbf{x}) = F_S(a,b,h,g) + F_L(a,b,h,g), \tag{15}$$

where $\mathbf{x} = \{a,b,h,g\}^{\mathsf{T}}$ is the vector of unknown dimensions of the PUC, $\overline{S}_{mm}$ and $\overline{L}_m$ are the values of L_m and S_{mm} functions corresponding to the target microstructure, parameters $i_{\max}$ and $j_{\max}$ define the range of points, in which S_{mm} functions are matched, N_d denotes the number of rays of a sampling template and $N_\ell(i)$ is the number of pixels of the i-th sampling ray, respectively. Then, the following optimization problem is to be solved in order to determine the optimal parameters of a periodic unit cell:

Optimal plain weave periodic unit cell. For a selected statistical descriptor $D \in \{S, L, S+L\}$ find the parameters of the PUC $\mathbf{x}$ such that

$$\mathbf{x} \in \operatorname*{Argmin}_{\mathbf{x} \in \mathcal{B}} F_D(\mathbf{x}), \tag{P}$$

where $\mathcal{B}$ denotes a set of admissible unit cell parameters,

$$\mathcal{B} = \left\{\mathbf{x} \in \mathbb{R}^4 : L_i \leq x_i \leq U_i, i = 1, \ldots, N\right\}, \tag{16}$$

where L_i and U_i denote the lower and upper bounds on unit cell parameters, selected, e.g., on the basis of image analysis.

The numerical experiments reported in [52] allow us to anticipate that the **RASA** algorithm, briefly described in the next section, is fully capable of solving this optimization problem.

3.3 Optimization algorithm

As demonstrated in [30,52], the objective functions (13)–(15) are discontinuous with a large number of local plateaus. This is a direct consequence of working with bitmap images with a limited resolution. Such objective functions cannot be directly treated by classical optimization algorithms. In our previous works [28,52,53], evolutionary algorithms showed themselves to be able to solve similar problems quite efficiently. Based on these results, the *Real-encoded Augmented Simulated Annealing* method is implemented to solve the present tasks. This method is the combination of two stochastic optimization techniques – genetic algorithm and the parallel simulated annealing [54]. It uses basic principles of genetic algorithms (a population of possible solutions (*individuals*), instead of one, is optimized, individuals are successively subjected to *selection* and recombination by *genetic operators* according to the value of their objective function (*fitness*)), but controls replacement of parents by the *Metropolis criterion* (see Eq. (18)). This increases the robustness of the method, since it allows a worse child to replace its parent and thus escape from local minima, which is in contradiction with the classical optimization methods. An interested reader may find further information on this subject, e.g., in [55,56]. The algorithmic scheme of the present implementation is briefly summarized as follows.

(1) Randomly generate an initial population and assign fitness to each individual. Initial temperature is set to $T_0 = T_{max} = \texttt{T\_frac} F_{avg}$ and minimal temperature is determined as $T_{min} = \texttt{T\_frac\_min} F_{avg}$, where F_{avg} is the average fitness value of the initial population.
(2) Select an appropriate genetic operator. Each operator is assigned a certain probability of selection.
(3) Select an appropriate number of individuals (according to the operator) and generate possible replacements. To select individuals, we apply the *normalized geometric ranking* scheme. The probability of selection of the i-th individual is given by

$$p_i = q'(1-\texttt{q})^{r-1},\ q' = \frac{\texttt{q}}{1-(1-\texttt{q})^{\texttt{P}}}, \tag{17}$$

where $\texttt{q}$ is the probability of selecting the best individual in the population, r is the rank of the i-th individual with respect to its fitness, and $\texttt{P}$ is the population size.
(4) Apply operators to selected parent(s) to obtain possible replacement(s).

4a Look for an identical individual in a population. If such an individual exists, it is replaced by a new one. This operation increases the diversity of a population and thus decreases the chance of falling into a local minimum.

4b Replace an old individual if

$$u(0,1) \leq \exp\left(F(I_{\text{old}}) - F(I_{\text{new}})\right)/T_t, \tag{18}$$

where $F(\cdot)$ is the fitness of a given individual, T_t is the actual temperature and $u(\cdot,\cdot)$ is a random number with the uniform distribution on a given interval.

(5) Steps 2–3 are performed until the number of successfully accepted individuals reaches `success_max` or selected number of steps reaches `counter_max`.

(6) Decrease temperature

$$T_{t+1} = \texttt{T\_mult}T_t.$$

If actual temperature T_{t+1} is smaller then `T_min`, perform *reannealing* – i.e. perform step #1 for one half of the population.

(7) Steps 2–6 are repeated until the termination condition is attained.

The detailed description of this algorithm, list of used operators as well as some tests of its performance can be found in [53,57]. See also [30] for values of individual parameters of this method for the current optimization problems.

4 Numerical experiments

In this section, the performance and robustness of the selected global optimization method is investigated for a set of carefully chosen optimization problems. First, the ability of the algorithm to determine the parameters of a periodic unit cell with known parameters is investigated. Then, optimal unit cells are generated for artificial microstructures exhibiting layer shifts observed in micrographs of real composites. Finally, the quality of the resulting periodic unit cell is judged from the point of view of effective elastic properties derived from the numerical homogenization procedure.

4.1 Identification problem

To test sensitivity of the optimization process with respect to the bitmap resolution, three different bitmaps with dimensions 128×16, 256×32 and 512×64 pixels were constructed for a unit cell corresponding to parameters $a = 10, h = 3, g = b = 1$. For each bitmap the optimization algorithm was run 20 times to minimize the influence of various random circumstances. The computation was terminated if the algorithm returned a value smaller than 10^{-6}

or if the number of objective function evaluations exceeded 50,000. Bounds of individual parameters were set to 50% and 200% of the target values. The S_{mm}-based objective function was considered first. The matching range $i_{\min}$–$i_{\max}$ and $j_{\min}$–$j_{\max}$, introduced in Eq. (13), was set to comply with the dimension of a unit cell. For each run, minimum and maximum values of searched geometric parameters were recorded. The results of this experiment are listed in Tables 1 and 2. In addition, Table 1 provides information on the average number of function calls and the relative time needed to complete the optimization run for individual bitmaps [1]. Notice that the optimization process converged for every run, which confirms the robustness of the **RASA** algorithm. A typical convergence progress of the optimization method, showing an average and the best individual in the population, is displayed, together with the PUC evolution, in Figs. 4a–b.

Bitmap	***Success***	***Number of func. eval.***			***Total time***
resolution	***rate***	Min	Avg	Max	[s]
128×16	20 / 20	1 106	2 826	6 321	116
256×32	20 / 20	2 336	3 542	5 320	1 016
512×64	20 / 20	2 716	4 581	12 457	6 648

Table 1
S_{mm}-based identification: Number of function evaluations

Resolution	$a_{\min}$	$a_{\max}$	$h_{\min}$	$h_{\max}$
128×16	9.8442	10.1010	2.9961	3.0119
256×32	9.9253	10.0217	2.9959	3.0020
512×64	9.9726	10.0259	2.9986	3.0009
Resolution	$b_{\min}$	$b_{\max}$	$g_{\min}$	$g_{\max}$
128×16	0.9924	1.0065	0.9688	1.1010
256×32	0.9968	1.0002	0.9831	1.0141
512×64	0.9988	1.0009	0.9917	1.0157

Table 2
Geometrical parameters of the PUC : S_{mm}-based optimization

In general, see Table 1, the number of required iterations as well as the time needed for convergence increases with the bitmap resolution. Nevertheless, all

[1] All reported tests were performed on a computer with Intel Celeron 700 MHz processor with 256MB RAM under the Linux operating system. The C++ code was compiled by **gcc 2.96** GNU complier with `-O3` optimization switch. The library **FFTW 2.1.3** [58] was called to compute the Fast Fourier Transform.

considered bitmap resolutions, at least for the present problem, provide comparable results in terms of accuracy of the searched geometric characteristics.

The similar numerical experiments were repeated for the F_L and F_{S+L} objective functions for the bitmap resolution 256×32 pixels. Note that sampling templates with parameters $T_W = T_H = H/2$ and $\Delta_W = \Delta_H = H/8$ were used for the determination of the lineal path function L_{mm}. The statistics of the obtained numerical parameters together with the number of function calls and overall computational time are stored in Tables 3 and 4. Note that both optimization problems, being based on the L_m function, are about ten times more time consuming. This again highlights the remarkable efficiency of the **FFTW** library. Furthermore, both objective functions result in geometrical parameters determined with a precision comparable to the S_{mm}-based optimization. This suggests that the scatter of the geometrical parameters is caused solely by the discretization of the microstructure not by the objective function or the selected optimization method.

Descriptor	***Success rate***	***Number of func. eval.***			***Total time***
		Min	Avg	Max	[s]
L_m	20 / 20	3 059	5 842	9 295	12 592
$L_m + S_{mm}$	20 / 20	1 196	4 909	30 699	11 804

Table 3
L_m and $L_m + S_{mm}$-based identification for 256×32 bitmap: Number of function evaluations

Descriptor	$a_{\min}$	$a_{\max}$	$h_{\min}$	$h_{\max}$
L_m	9.9227	10.0407	2.9967	3.0020
$L_m + S_{mm}$	9.9243	10.0196	2.9977	3.0023
Descriptor	$b_{\min}$	$b_{\max}$	$g_{\min}$	$g_{\max}$
L_m	0.9973	1.0005	0.9855	1.0143
$L_m + S_{mm}$	0.9969	1.0009	0.9864	1.0139

Table 4
Geometrical parameters of the PUC for 256×32 bitmap: L_m-based optimization, combined optimization

Finally, for the sake of completeness, examples of typical objective runs together with the plot of objective functions are shown in Figs. 4.

To summarize this study, the presented results support the choice of the selected optimization method; furthermore, the resolution of the bitmap 256×32 is sufficient to obtain the searched geometrical parameters with a reasonable precision.

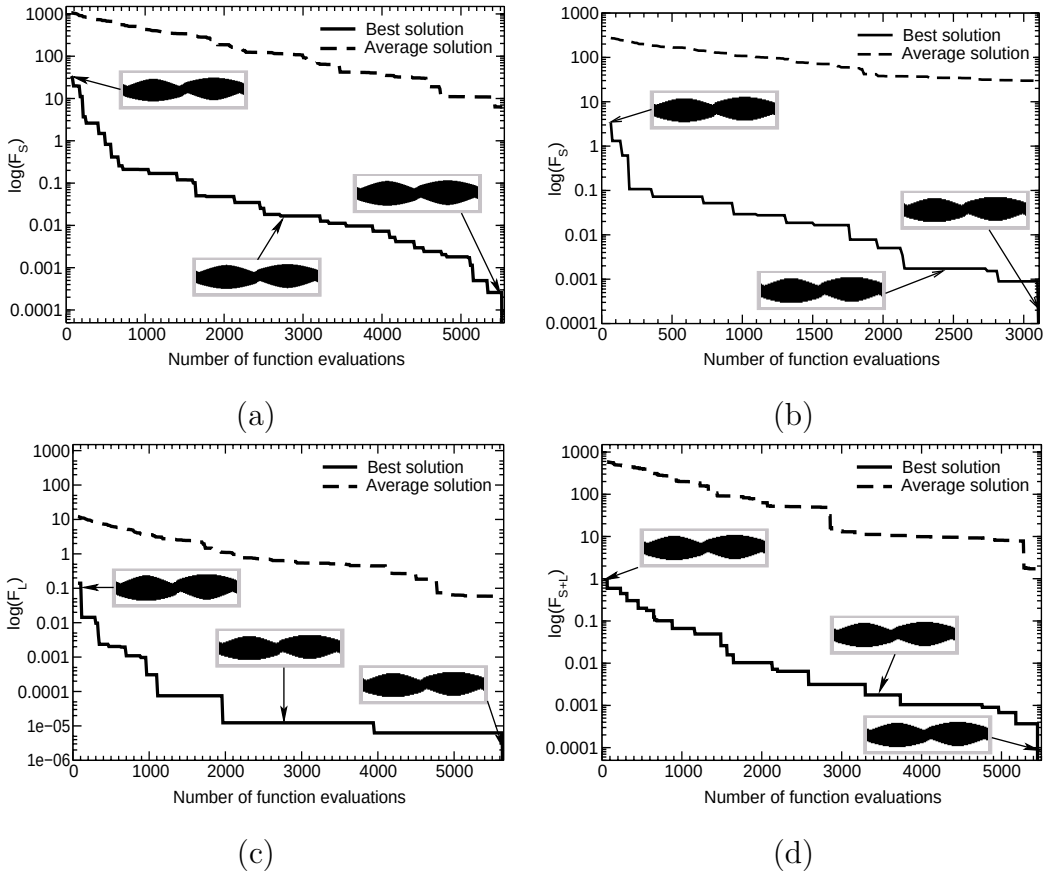

Fig. 4. Examples of typical optimization procedures, (a) S_{mm}-based objective function, bitmap resolution 512×64 pixels, (b) S_{mm}-based objective function, bitmap resolution 256×32 pixels, (c) L_m-based objective function, bitmap resolution 256×32 pixels, (d) $(S_{mm} + L_m)$-based objective function, bitmap resolution 256×32 pixels

4.2 Woven composites with shifted layers

As a representative of digitized images of real-world multilayered plain weave composites, a set of three artificial bitmaps exhibiting different imperfections was generated. In particular, the "samples" formed by two unit cells with different layer and bundle heights (see Fig. 5b), two identical unit cells shifted by a (see Fig. 5c) and by $a/2$ (see Fig. 5d) are considered in this section [2]. Based on the results of the sensitivity analysis in the previous section, the PUC #1 was discretized as a bitmap with the dimensions 256×92 pixels and the PUC #2–3 were represented by bitmaps with resolution 256×64 pixels.

For each artificial mesostructure bitmap, the statistically optimal periodic unit

[2] The parameters of the bitmap 5b are $a = 10, h = 3, b = g = 1$ for the lower layer and $a = 10, h = 4.5, b = 1.5, g = 1$ for the upper one; the remaining bitmaps correspond to a unit cell with $a = 10, h = 3, b = g = 1$.

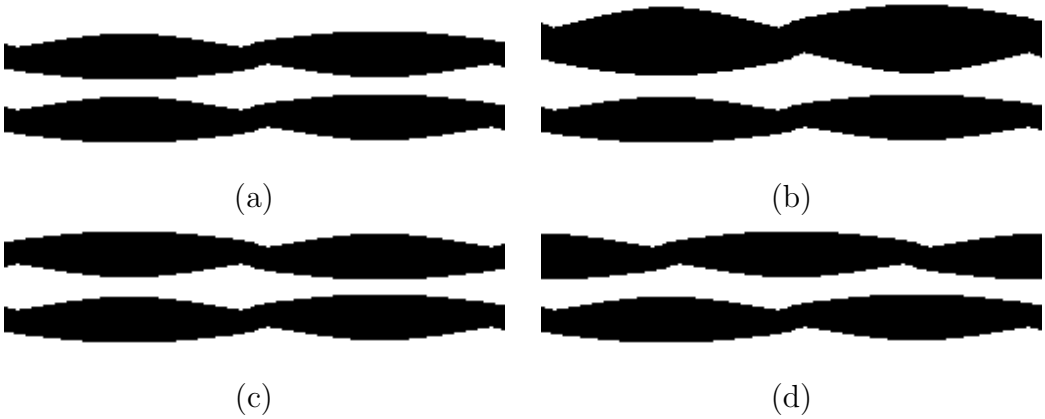

Fig. 5. Artificial bitmaps of mesoscale geometry with typical tow misalignments, (a) ideal stacking, (b) different layer heights (PUC #1), (c) layers shifted by a (PUC #2), (d) layers shifted by $a/2$ (PUC #3)

cell based on S_{mm}, L_m and $S_{mm} + L_m$ descriptors was found. The target value of the objective function for each optimization problem was set to 10^{-6} and the maximum number of function evaluations was restricted to 25,000. Each optimization problem was executed ten times to verify that the global optimum was reached and to determine the scatter of geometrical parameters. The resulting optimal values obtained for individual bitmaps are stored in Table 5. As expected, the values of identified parameters differ for individual statistical descriptors. The reliability of the optimization process is rather ecouraging, particularly when judging from the precision of the identified parameters for combined objective function.

4.3 Homogenization

In the next step, optimized parameters derived in previous sections are used in the geometrical model of Fig. 5 to generate an equivalent periodic unit cell that represents a real composite. Such a unit cell can be then used within the framework of the finite element method-based homogenization to arrive at the desired approximation of the effective material behavior. Although a variety of works devoted to this topic can be found in the literature, see, e.g., [8,9,14,59–62] the homogenization procedure for the "stress-control" problem, in the terminology of Michel et.al [60], is briefly reviewed here for the sake of completeness.

4.3.1 Problem formulation

To introduce the subject, consider a plain weave composite PUC with the local coordinate systems defined such that the local x_1^ℓ axis is aligned with

Periodic Unit Cell #1				
Descriptor	a	h	b	g
S_{mm}	10.235 ± 0.023	3.792 ± 0.002	1.250 ± 0.001	1.726 ± 0.012
L_m	10.316 ± 0.018	3.785 ± 0.003	1.252 ± 0.001	1.766 ± 0.016
$S_{mm} + L_m$	10.098 ± 0.015	3.754 ± 0.000	1.249 ± 0.000	1.014 ± 0.005
Periodic Unit Cell #2				
Descriptor	a	h	b	g
S_{mm}	9.931 ± 0.017	2.964 ± 0.001	0.995 ± 0.001	0.990 ± 0.005
L_m	10.863 ± 0.023	2.956 ± 0.002	0.996 ± 0.001	1.013 ± 0.008
$S_{mm} + L_m$	9.975 ± 0.004	2.964 ± 0.001	0.994 ± 0.001	0.988 ± 0.005
Periodic Unit Cell #3				
Descriptor	a	h	b	g
S_{mm}	11.171 ± 0.032	3.046 ± 0.001	0.996 ± 0.001	0.670 ± 0.012
L_m	8.351 ± 0.033	2.887 ± 0.003	0.964 ± 0.001	0.247 ± 0.012
$S_{mm} + L_m$	10.841 ± 0.016	3.045 ± 0.001	0.998 ± 0.001	0.715 ± 0.007

Table 5
Geometrical parameters of mesoscale PUCs

the fiber direction. Further suppose that the PUC is subjected to a prescribed overall stress $\boldsymbol{\Sigma}$. Due to assumed periodicity of the microstructure, the local displacement field $\mathbf{u}(\mathbf{x})$ on mesoscale admits the following decomposition

$$\mathbf{u}(\mathbf{x}) = \boldsymbol{E} \cdot \mathbf{x} + \mathbf{u}^*(\mathbf{x}), \tag{19}$$

where $\mathbf{u}^*(\mathbf{x})$ represents a periodic fluctuation of the local displacement field due to the presence of heterogeneities and $\boldsymbol{E}$ is the overall strain tensor. The local strain tensor then assumes the form

$$\boldsymbol{\varepsilon}(\mathbf{x}) = \boldsymbol{E} + \boldsymbol{\varepsilon}^*(\mathbf{x}), \tag{20}$$

where the fluctuating part $\boldsymbol{\varepsilon}^*(\mathbf{x})$ vanishes under volume averaging. The goal now becomes the evaluation of local fields within the mesoscopic unit cell and then their averaging to receive at the searched macroscopic response. In doing so, we first write the principle of virtual work (the Hill-Mandel lemma) in the form

$$\begin{aligned} \delta\boldsymbol{E} : \boldsymbol{\Sigma} &= \langle \delta\boldsymbol{\varepsilon}(\mathbf{x}) : \boldsymbol{\sigma}(\mathbf{x}) \rangle = \left\langle \delta\boldsymbol{\varepsilon}^\ell(\mathbf{x}) : \boldsymbol{\sigma}^\ell(\mathbf{x}) \right\rangle \\ &= \left\langle \left(\delta\boldsymbol{E}^\ell + \delta\boldsymbol{\varepsilon}^\ell(\mathbf{x}) \right) : \boldsymbol{\sigma}^\ell(\mathbf{x}) \right\rangle, \end{aligned} \tag{21}$$

where $\langle\cdot\rangle$ now denotes averaging with respect to the PUC and $\cdot^{\ell}$ is used to denote a quantity in a local coordinate system. The stress field written in the local coordinate system then reads

$$\boldsymbol{\sigma}^{\ell}(\mathbf{x}) = \mathbf{L}^{\ell}(\mathbf{x}) : \left(\boldsymbol{E}^{\ell} + \boldsymbol{\varepsilon}^{*\ell}(\mathbf{x})\right), \tag{22}$$

with $\boldsymbol{\sigma}^{\ell}(\mathbf{x})$ standing for the local stress field, $\mathbf{L}^{\ell}$ is the material stiffness tensor. Relating the strain tensors in the local and global coordinate systems by well-known relations $\boldsymbol{E}^{\ell} = \mathbf{T}_{\varepsilon} : \boldsymbol{E}$, $\boldsymbol{\varepsilon}^{*\ell} = \mathbf{T}_{\varepsilon} : \boldsymbol{\varepsilon}^{*}$, see, e.g. [41], and inserting Eq. (22) into Eq. (21) yields the stationarity conditions of a given problem in the form

$$\delta\boldsymbol{E} : \boldsymbol{\Sigma} = \delta\boldsymbol{E} : \left\langle \mathbf{T}_{\varepsilon}(\mathbf{x}) : \left[\mathbf{L}^{\ell}(\mathbf{x}) : \mathbf{T}_{\varepsilon}(\mathbf{x}) : \left(\boldsymbol{E} + \boldsymbol{\varepsilon}^{*}(\mathbf{x})\right)\right]\right\rangle, \tag{23}$$

$$0 = \left\langle \delta\boldsymbol{\varepsilon}^{*}(\mathbf{x}) : \mathbf{T}_{\varepsilon}(\mathbf{x}) : \left[\mathbf{L}^{\ell}(\mathbf{x}) : \mathbf{T}_{\varepsilon}(\mathbf{x}) : \left(\boldsymbol{E} + \boldsymbol{\varepsilon}^{*}(\mathbf{x})\right)\right]\right\rangle, \tag{24}$$

has to be satisfied for all kinematically admissible variations $\delta\boldsymbol{E}$ and $\delta\boldsymbol{\varepsilon}^{*}$.

4.3.2 Discretization

To obtain an approximate solution of the above system of equations, the standard conforming finite element method discretization is employed. We start from decomposing the mesoscale periodic unit cell Y into N_e disjoint elements Y_e with the discretization respecting the interfaces between individual tows and the matrix phase. Employing the engineering notation [41,42], the approximation of the fluctuating part of the displacement field $\mathbf{u}^{*}$, written in the *global* coordinate system, yields

$$\{\mathsf{u}^{*}(\mathbf{x})\} = [\mathsf{N}(\mathbf{x})]\,\{\mathsf{r}\}, \tag{25}$$

where $[\mathsf{N}]$ represents, as usual, the matrix of shape functions for a given partition of the unit cell and $\{\mathsf{r}\}$ is the vector of unknown degrees of freedom. The corresponding approximation of the strain field is then provided by

$$\{\varepsilon(\mathbf{x})\} = \{\mathsf{E}\} + [\mathsf{B}(\mathbf{x})]\,\{\mathsf{r}\}, \tag{26}$$

where $[\mathsf{B}]$ is the strain-displacement matrix. Introducing Eq. (26) into Eq. (21) gives, for any kinematically admissible strains $\{\delta\varepsilon^{*}\} = [\mathsf{B}]\,\{\delta\mathsf{r}\}$ and $\{\delta\mathsf{E}\}$, we get the associated system of linear equations in the form

$$\begin{bmatrix} \mathsf{K}_{11} & \mathsf{K}_{12} \\ \mathsf{K}_{12}{}^{\mathsf{T}} & \mathsf{K}_{22} \end{bmatrix} \begin{Bmatrix} \mathsf{E} \\ \mathsf{r} \end{Bmatrix} = \begin{Bmatrix} \Sigma \\ 0 \end{Bmatrix}. \tag{27}$$

The individual stiffness matrices and vectors of generalized nodal forces are obtained by the assembly of contributions for individual elements,

$$[\mathsf{K}_{11}] = \mathop{\mathsf{A}}_{e=1}^{N_e} [\mathsf{K}_{11,\mathsf{e}}], \text{where } [\mathsf{K}_{11,\mathsf{e}}] = \frac{1}{|Y|} \int_{Y_e} [\mathsf{T}_{\varepsilon,\mathsf{e}}]^{\mathsf{T}} \left[\mathsf{L}^{\ell}_{\text{meso},\mathsf{e}}\right] \, \mathrm{d}Y_e, \tag{28}$$

$$[\mathsf{K}_{12}] = \mathop{\mathsf{A}}_{e=1}^{N_e} [\mathsf{K}_{12,\mathsf{e}}], \text{where } [\mathsf{K}_{12,\mathsf{e}}] = \frac{1}{|Y|} \int_{Y_e} [\mathsf{T}_{\varepsilon,\mathsf{e}}]^{\mathsf{T}} \left[\mathsf{L}^{\ell}_{\text{meso},\mathsf{e}}\right] \left[\widehat{\mathsf{B}}_{\mathsf{e}}\right] \, \mathrm{d}Y_e,$$

$$[\mathsf{K}_{22}] = \mathop{\mathsf{A}}_{e=1}^{N_e} [\mathsf{K}_{22,\mathsf{e}}], \text{where } [\mathsf{K}_{22,\mathsf{e}}] = \frac{1}{|Y|} \int_{Y_e} \left[\widehat{\mathsf{B}}_{\mathsf{e}}\right]^{\mathsf{T}} \left[\mathsf{L}^{\ell}_{\text{meso},\mathsf{e}}\right] \left[\widehat{\mathsf{B}}_{\mathsf{e}}\right] \, \mathrm{d}Y_e,$$

where the "rotated" displacement-strain matrix $\left[\widehat{\mathsf{B}}_{\mathsf{e}}\right]$ is defined by the relation $\left[\widehat{\mathsf{B}}_{\mathsf{e}}\right] = [\mathsf{T}_{\varepsilon,\mathsf{e}}] [\mathsf{B}_{\mathsf{e}}]$ and A stands for the assembly of contribution of individual elements [41,42]. The local-global transformation can be, e.g., easily parametrized by Euler angles determined from relations (A.10)–(A.11). Note that in the present implementation, linear tetrahedral elements are used and the values of Euler angles are related to the center of gravity of each element and are supposed to remain constant on a given element. Furthermore, the periodicity condition for the fluctuating field $\mathbf{u}^*$ was accounted for through multi-point constraints, see [60].

Finally, eliminating the fluctuating displacements from the system (27) allows us to write the homogenized constitutive law in the form

$$\{\Sigma\} = \left[\mathsf{L}^{\mathsf{fem}}\right] \{\mathsf{E}\}, \text{where } \left[\mathsf{L}^{\mathsf{fem}}\right] = [\mathsf{K}_{11}] - [\mathsf{K}_{12}] [\mathsf{K}_{22}]^{-1} [\mathsf{K}_{12}]^{\mathsf{T}}. \tag{29}$$

An important step of the mesoscale modeling is preparation of a 3D mesh of warp and fill bundles and matrix phase complying with the requirements of mesh periodicity. In the current work, the principles of matched mesh generation [63] were implemented into Advancing Front method-based automated mesh generator **T3D** [64,65]. Examples of tetrahedral meshes of a plain-weave unit cell generated by this algorithm are displayed in Figs. 6 and 7.

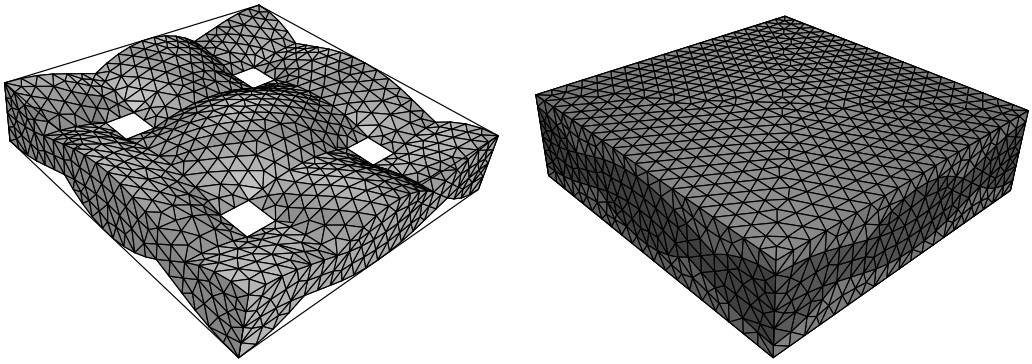

Fig. 6. Plain weave finite element meshes

4.4 Results

As the first step, the effect of scatter of individual identified parameters is addressed. The material properties of matrix and bundle were taken from [28] and are listed in Table 6.

Bundle properties [GPa]								
L^{ℓ}_{11}	L^{ℓ}_{22}	L^{ℓ}_{33}	L^{ℓ}_{12}	L^{ℓ}_{13}	L^{ℓ}_{23}	L^{ℓ}_{44}	L^{ℓ}_{55}	L^{ℓ}_{66}
176.8	10.74	10.72	6.897	6.897	6.319	2.216	4.861	4.861

Matrix properties [GPa]			
E_A	E_T	G_T	ν_A
5.5	5.5	1.96	0.40

Table 6
Elastic material properties

The minimum and maximum dimensions were taken from the S_{mm}-based identification problem for the bitmap dimensions 256×32, see Table 2. The results stored in Table 7 show that the difference in effective elastic moduli due to uncertainty in mesoscale PUC parameters is approximately comparable to the differences found by uniform mesh refinement [30]. Moreover, the deviation of the $\mathsf{L}^{\mathsf{fem}}{}_{11}$ entry can be attributed to a relatively large difference in the bundle volume fraction c_f for the analyzed unit cells.

Dimensions	$\mathsf{L}^{\mathsf{fem}}{}_{11}$ [GPa]	$\mathsf{L}^{\mathsf{fem}}{}_{12}$ [GPa]	$\mathsf{L}^{\mathsf{fem}}{}_{33}$ [GPa]	$\mathsf{L}^{\mathsf{fem}}{}_{44}$ [GPa]	$\mathsf{L}^{\mathsf{fem}}{}_{66}$ [GPa]	c_f
Minimal	25.247	7.496	11.371	2.264	2.965	0.3674
Target	25.250	7.494	11.370	2.265	2.966	0.3678
Maximal	25.217	7.508	11.384	2.247	2.922	0.3554

Table 7
Effects of uncertainties in mesoscale PUC dimensions

Finally, we present the comparison of effective elastic properties for the target bitmaps and corresponding statistically optimized unit cells obtained in Section 4.2. The finite element meshes corresponding to the target mesostructure appear in Fig. 7[3], while the effective elastic properties of the target microstructure and the statistically optimized unit cells are stored in Table 8.

Evidently, the best correspondence between the artificial micrographs and the

[3] Note that for mesh generation, the unit cells were shifted by $a/2$ compared to bitmaps displayed in Fig. 5.

Periodic Unit Cell #1						
Descriptor	$\mathsf{L}^{\mathsf{fem}}{}_{11}$ [GPa]	$\mathsf{L}^{\mathsf{fem}}{}_{12}$ [GPa]	$\mathsf{L}^{\mathsf{fem}}{}_{33}$ [GPa]	$\mathsf{L}^{\mathsf{fem}}{}_{44}$ [GPa]	$\mathsf{L}^{\mathsf{fem}}{}_{66}$ [GPa]	c_f
S_{mm}	21.100	7.499	11.401	2.265	2.868	0.3386
L_m	22.698	7.503	11.410	2.235	2.842	0.3312
$S_{mm} + L_m$	23.334	7.490	11.383	2.255	2.925	0.3567
Target	23.324	7.453	11.384	2.269	2.963	0.3678
Periodic Unit Cell #2						
Descriptor	$\mathsf{L}^{\mathsf{fem}}{}_{11}$ [GPa]	$\mathsf{L}^{\mathsf{fem}}{}_{12}$ [GPa]	$\mathsf{L}^{\mathsf{fem}}{}_{33}$ [GPa]	$\mathsf{L}^{\mathsf{fem}}{}_{44}$ [GPa]	$\mathsf{L}^{\mathsf{fem}}{}_{66}$ [GPa]	c_f
S_{mm}	25.341	7.500	11.375	2.257	2.947	0.3635
L_m	26.309	7.494	11.372	2.259	2.959	0.3671
$S_{mm} + L_m$	25.121	7.495	11.376	2.256	2.956	0.3629
Target	24.786	7.467	11.370	2.266	2.965	0.3678
Periodic Unit Cell #3						
Descriptor	$\mathsf{L}^{\mathsf{fem}}{}_{11}$ [GPa]	$\mathsf{L}^{\mathsf{fem}}{}_{12}$ [GPa]	$\mathsf{L}^{\mathsf{fem}}{}_{33}$ [GPa]	$\mathsf{L}^{\mathsf{fem}}{}_{44}$ [GPa]	$\mathsf{L}^{\mathsf{fem}}{}_{66}$ [GPa]	c_f
S_{mm}	27.629	7.471	11.362	2.268	2.997	0.3752
L_m	27.464	7.393	11.349	2.279	3.027	0.3872
$S_{mm} + L_m$	27.095	7.473	11.371	2.258	2.966	0.3678
Target	24.694	7.416	11.374	2.273	2.972	0.3670

Table 8
Effective properties of statistically optimized mesoscale PUCs

periodic unit cell was reached for the PUC #1 microstructure where the optimization procedure predicts the in-plane properties with approximately the same variation as the one resulting from uniform mesh size refinement [30]. Note that analogously to problems of random media reconstruction, the combined optimization procedure yields the best results. The periodic unit cell based on parameters identified for PUC #2 correctly predicts the bundle volume fraction; it does not, however, take into account the different inclination of tows in individual layers which results in a slight overestimation of $\mathsf{L}^{\mathsf{fem}}{}_{11}$ modulus. The most severe differences can be observed for the PUC #3 microstructure. As follows from Table 5, all the optimized unit cell exhibit substantially smaller value of gap between individual tows g to accommodate the layer shift present in the target micrograph, which leads to overestimating the

bundle volume fraction resulting in a higher value of the in-plane component $\mathsf{L}^{\mathsf{fem}}{}_{11}$.

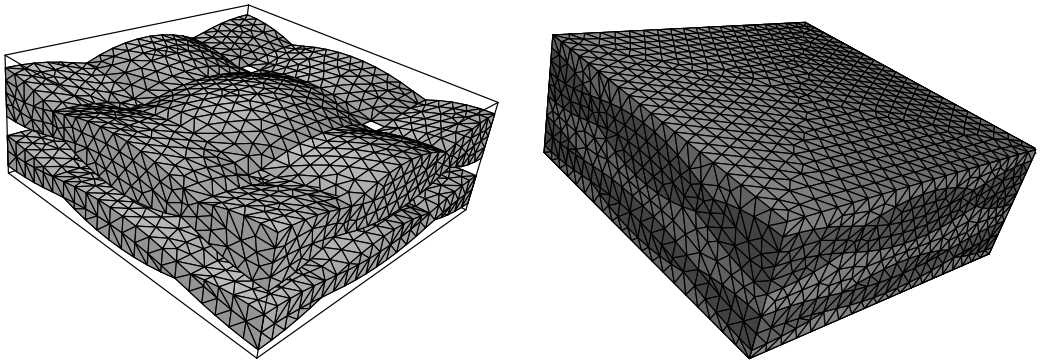

(a)

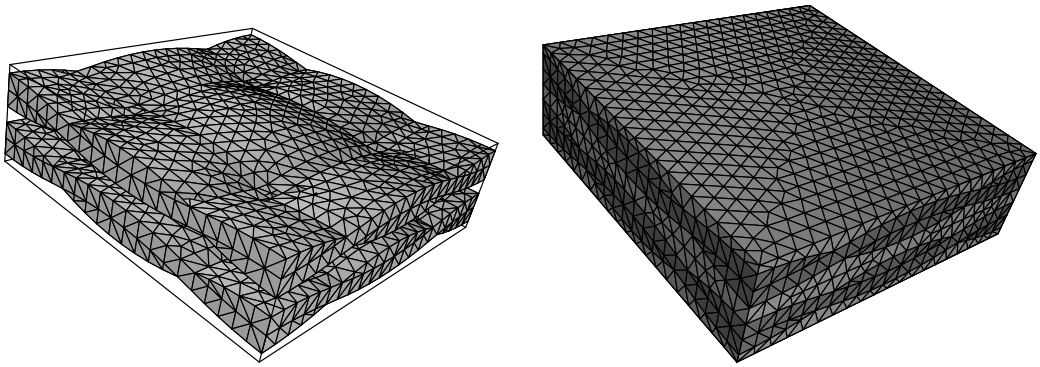

(b)

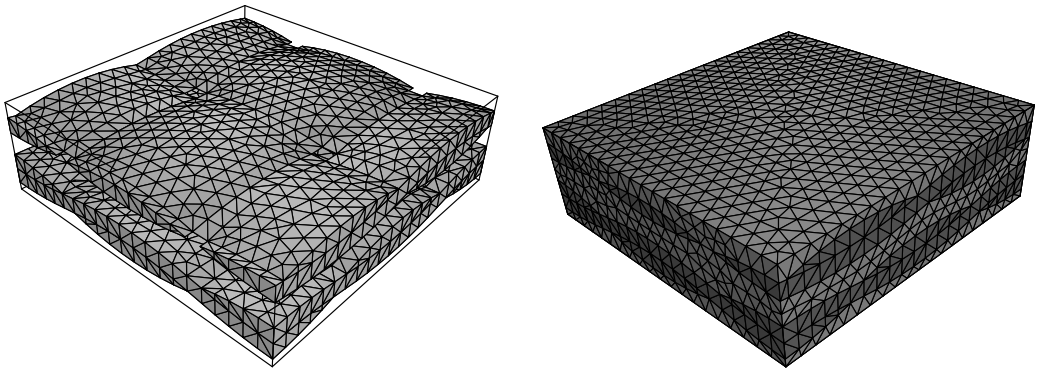

(c)

Fig. 7. Mesoscale meshes, (a) PUC #1, (b) PUC #2, (c) PUC #3

5 Conclusions

In the first part of the present work, a simple and intuitive approach to the determination of idealized periodic unit cells based on microstructural statistics

has been proposed. In particular, the reconstruction based on the two-point probability function, the lineal path function and their combination has been considered. The applicability and limitations of the present procedure have been demonstrated by analyzing artificial binary images of two-layer composite materials with relative shift of individual layers. The geometrical parameters of the periodic unit cells, following from the optimization analysis, have been employed to formulate the Finite Element model and to determine the effective elastic properties of the resulting composite.

The obtained results allow us to conclude that the proposed procedure can be efficiently used for multilayered composites with possibly varying layers heights provided that the relative shift of individual layers is not very large or approximately equal to the unit cell half-width. In the opposite case, however, it appears to be necessary to formulate the optimized unit cell in terms of at least two-layered composite, too. Note, however, that the difference of cross-sections corresponding to planes $x = \pm a$ and $y = \pm a$, see Fig. 7c, calls for microstructural information supplied in the form of bitmaps taken from several locations of a composite in two orthogonal directions rather than for only one bitmap considered in this work. This generalization, together with the examples of real-world microstructures, will be considered in the forthcoming second part of this paper [66].

Acknowledgements

We would like to express our thanks to Dr. Daniel Rypl for numerous discussions and support while solving problems of mesh generation. The financial support of this work provided by CAĞR grants No. 106/03/0180 and No. 103/01/D052 is gratefully acknowledged.

References

[1] T. Ishikawa, T. Chou, Elastic behavior of woven hybrid composites, Journal of Composite Materials 16 (1982) 2–19.

[2] T. Ishikawa, T. Chou, Stiffness and strength behavior of woven fabric composites, Journal of Materials Science 17 (11) (1982) 3211–3220.

[3] N. Naik, P. Shembekar, Elastic behavior of woven fabric composites. 1. Lamina analysis, Journal of Composite Materials 26 (15) (1992) 2196–2225.

[4] A. Kregers, Y. Malbardis, Determination of the deformability of three-dimensionally reinforced composites by stiffness averaging method, Polymer Mechanics 1 (1) (1978) 3–8.

[5] C. Pastore, Y. Gowayed, A self-consistent fabric geometry model - modification and application of a fabric geometry model to predict the elastic properties of textile composites, Journal of Composites Technology & Research 16 (1) (1994) 32–36.

[6] B. Gommers, I. Verpoest, P. Van Houtte, The Mori-Tanaka method applied to textile composite materials, Acta Materialia 46 (6) (1998) 2223–2235.

[7] Y. Zhang, J. Harding, A numerical micromechanics analysis of the mechanical properties of a plain weave composite, Computers & Structures 36 (5) (1990) 839–844.

[8] P. Paumelle, A. Hassim, F. Léné, Composites with woven reinforcements : Calculation and parameter analysis of the properties of the homogeneous equivalent, Recherche Aerospatiale 1 (1990) 1–12.

[9] P. Paumelle, A. Hassim, F. Léné, Microstress analysis in woven composite structure, Recherche Aerospatiale 6 (1991) 47–62.

[10] A. Dasgupta, S. Bhandarkar, Effective thermomechanical behavior of plain-weave fabric-reinforced composites using homogenization theory, Journal of Engineering Materials and Technology-Transactions of the ASME 116 (1) (1994) 99–105.

[11] C. Chapman, J. Whitcomb, Effect of assumed tow architecture on predicted moduli and stresses in plain weave composites, Journal of Composite Materials 29 (16) (1995) 2134–2159.

[12] J. Whitcomb, K. Sriregan, Effect of various approximations on predicted progressive failure in plain weave composites, Composite Structures 34 (1) (1996) 13–20.

[13] B. Cox, G. Flanagan, Handbook of analytical methods for textile composites, NASA Contractor Report 4750, Langley Research Center, `http://techreports.larc.nasa.gov/ltrs` (1997).

[14] J. Byström, N. Jekabsons, J. Varna, An evaluation of different models for prediction of elastic properties of woven composites, Composites Part B: Engineering 31 (1) (2000) 7–20.

[15] P. W. Chung, K. K. Tamma, Woven fabric composites - developments in engineering bounds, homogenization and applications, International Journal for Numerical Methods in Engineering 45 (12) (1999) 1757–1790.

[16] K. Breiling, D. Adams, Effects of layer nesting on compression-loaded 2-D woven textile composites, Journal of Composite Materials 30 (15) (1996) 1710–1728.

[17] M. Košek, B. Košková, Analysis of yarn wavy path periodicity of textile composites using Discrete Fourier Transform, in: Proceeding of International Conference on Composite Engineering ICCE/6, Orlando, Florida, 1999, pp. 427–429.

[18] B. Košková, S. Vopička, Determination of yarn waviness parameters for C/C woven composites, in: Proceedings of International Conference CARBON '01, Lexington (KY,USA), 2001, pp. 1–6.

[19] A. K. Roy, Comparison of in situ damage assessment in unbalanced fabric composite and model laminate of planar (one-directional) crimping, Composites Science and Technology 58 (11) (1998) 1793–1801.

[20] S. Yurgartis, K. Morey, J. Jortner, Measurement of yarn shape and nesting in plain-weave composites, Composites Science and Technology 46 (1) (1993) 39–50.

[21] C. Pastore, Quantification of processing artifacts in textile composites, Composites Manufacturing 4 (4) (1993) 217–226.

[22] P. Shembekar, N. Naik, Elastic behavior of woven fabric composites. 2. Laminate analysis, Journal of Composite Materials 26 (15) (1992) 2226–2246.

[23] S. P. Yushanov, A. E. Bogdanovich, Stochastic theory of composite materials with random waviness of the reinforcements, International Journal of Solids and Structures 35 (22) (1998) 2901–2930.

[24] S. P. Yushanov, A. E. Bogdanovich, Fiber waviness in textile composites and its stochastic modeling, Mechanics of Composite Materials 36 (4) (2000) 297–318.

[25] K. Woo, J. D. Whitcomb, Effects of fiber tow misalignment on the engineering properties of plain weave textile composites, Composite Structures 37 (3–4) (1997) 281–417.

[26] N. Jekabsons, J. Byström, On the effect of stacked fabric layers on the stiffness of a woven composite, Composites Part B: Engineering 33 (8) (2002) 619–629.

[27] G. L. Povirk, Incorporation of microstructural information into models of two-phase materials, Acta metallurgica et materialia 43 (8) (1995) 3199–3206.

[28] J. Zeman, M. Šejnoha, Numerical evaluation of effective properties of graphite fiber tow impregnated by polymer matrix, Journal of the Mechanics and Physics of Solids 49 (1) (2001) 69–90.

[29] M. Šejnoha, J. Zeman, Overall viscoelastic response of random fibrous composites with statistically quasi uniform distribution of reinforcements, Computer Methods in Applied Mechanics and Engineering 191 (44) (2002) 5027–5044.

[30] J. Zeman, Analysis of composite materials with microstructure imperfections, Ph.D. thesis, Klokner Institute, Czech Technical University in Prague (2003).

[31] S. Jia, G. Raiser, G. Povirk, Modeling the effects of hole distribution in perforated aluminum sheets i: Representative unit cells, International Journal of Solids and Structures 39 (9) (2002) 2517–2532.

[32] J. L. Kuhn, P. G. Charalambides, Modeling of plain weave fabric composite geometry, Journal of Composite Materials 33 (3) (1999) 188–220.

[33] M. Rintoul, S. Torquato, Reconstruction of the structure of dispersions, Journal of Colloid and Interface Science 186 (2) (1997) 467–476.

[34] C. L. Y. Yeong, S. Torquato, Reconstructing random media, Physical Review E 57 (1) (1998) 495–506.

[35] C. L. Y. Yeong, S. Torquato, Reconstructing random media. II. Three-dimensional media from two-dimensional cuts, Physical Review E 58 (1) (1998) 224–233.

[36] C. Mahwart, S. Torquato, R. Hilfer, Stochastic reconstruction of sandstones, Physical Review E 62 (1) (2000) 893–899.

[37] M. Talukdar, O. Torsaeter, M. Ionnidis, Stochastic reconstruction of particulate media from two-dimensional images, Journal of Colloid and Interphase Science 248 (2) (2002) 419–428.

[38] D. Cule, S. Torquato, Generating random media from limited microstructural information via stochastic optimization, Journal of Applied Physics 86 (6) (1999) 3428–3437.

[39] N. Sheehan, S. Torquato, Generating microstructures with specified correlation functions, Journal of Applied Physics 89 (1) (2001) 53–60.

[40] M. G. Rozman, M. Utz, Efficient recontruction of multiphase morphologies from corellation functions, Physical Review E 63 (2001) 066701–1–066701–8.

[41] Z. Bittnar, J. Šejnoha, Numerical methods in structural engineering, ASCE Press, 1996.

[42] K. J. Bathe, Finite Element Procedures, 2nd Edition, Prentice Hall, 1995.

[43] S. Torquato, Random heterogeneous materials: Microstucture and macroscopic properties, Springer-Verlag, 2002.

[44] S. Torquato, G. Stell, Microstructure of two-phase random media.I. The n-point probability functions, Journal of Chemical Physics 77 (4) (1982) 2071–2077.

[45] P. Smith, S. Torquato, Computer simulation results for the two-point probability function of composite media, Journal of Computational Physics 76 (1988) 176–191.

[46] J. G. Berryman, Measurement of spatial correlation functions using image processing techniques, Journal of Applied Physics 57 (7) (1984) 2374–2384.

[47] B. Lu, S. Torquato, Lineal-path function for random heterogeneous materials, Physical Review E 45 (2) (1992) 922–929.

[48] M. Li, S. Ghosh, T. N. Rouns, H. Weiland, O. Richmond, W. Hunt, Serial sectioning method in the construction of 3-D microstructures for particle-reinforced MMCs, Materials Characterization 41 (2–3) (1998) 81–95.

[49] G. Nagai, T. Yamada, A. Wada, Accurate modeling and fast solver for the stress analysis of concrete materials based on digital image processing technique, International Journal for Computational Civil and Structural Engineering 1.

[50] K. Terada, T. Miura, N. Kikuchi, Digital image-based modeling applied to the homogenization analysis of composite materials, Computational Mechanics 20 (4) (1997) 331–346.

[51] A. Roberts, E. Garboczi, Elastic properties of a tungsten-silver composite by reconstruction and computation, Journal of the Mechanics and Physics of Solids 47 (10) (1999) 2029–2055.

[52] J. Zeman, M. Šejnoha, On determination of periodic unit cell for plain weave fabric composites, Engineering Mechanics 1–2 (9) (2002) 65–74.

[53] K. Matouš, M. Lepš, J. Zeman, M. Šejnoha, Applying genetic algorithms to selected topics commonly encountered in engineering practice, Computer Methods in Applied Mechanics and Engineering 190 (13–14) (2000) 1629–1650.

[54] S. Mahfoud, D. Goldberg, Parallel recombinative simulated annealing: A genetic algorithm, Parallel Computing 21 (1) (1995) 1–28.

[55] D. Goldberg, Genetic Algorithms in Search, Optimization and Machine Learning, Addison-Wesley, 1989.

[56] Z. Michalewicz, Genetic Algorithms + Data Structures = Evolution Programs, 3rd Edition, Springer-Verlag, 1996.

[57] O. Hrstka, A. Kučerová, M. Lepš, J. Zeman, A competitive comparison of different types of evolutionary algorithms, Computers & Structures In press.

[58] M. Erigo, S. Johnson, FFTW: An adaptive software architecture for the FFT, in: Proceedings of the 1998 IEEE International Conference on Acoustics, Speech and Signal Processing, ICASSP98, Vol. 3, IEEE, New York, 1998, pp. 1381–1384, (See also `http://www.fftw.org`).

[59] K. Woo, J. D. Whitcomb, A post-processor approach for stress analysis of woven textile composites, Composites Science and Technology 60 (5) (2000) 693–704.

[60] J. C. Michel, H. Moulinec, P. Suquet, Effective properties of composite materials with periodic microstructure: A computational approach, Computer Methods in Applied Mechanics and Engineering 172 (1999) 109–143.

[61] J. Guedes, N. Kikuchi, Preprocessing and postprocessing for materials based on the homogenization method with adaptive finite elements method, Computer Methods in Applied Mechanics and Engineering 83 (2) (1991) 143–198.

[62] V. Kouznetsova, W. A. M. Brekelmans, P. T. Baaijens, An approach to micro-macro modeling of heterogeneous materials, Computational Mechanics 27 (1) (2001) 37–48.

[63] R. Wentorf, R. Collar, M. S. Shephard, J. Fish, Automated modeling for complex woven mesostructures, Computer Methods in Applied Mechanics and Engineering 172 (1–4) (1999) 273–291.

[64] D. Rypl, Sequential and parallel generation of unstructured 3D meshes, Vol. 2 of CTU Reports, Czech Technical University in Prague, 1998.

[65] D. Rypl, T3D program homepage, ksm.fsv.cvut.cz/~dr/t3d.html

[66] B. Tomková, M. Šejnoha, J. Zeman, Homogenization of plain weave composites with imperfect microstructure: Part ii – analysis of real-world materials, in preparation.

A Woven composite geometrical model

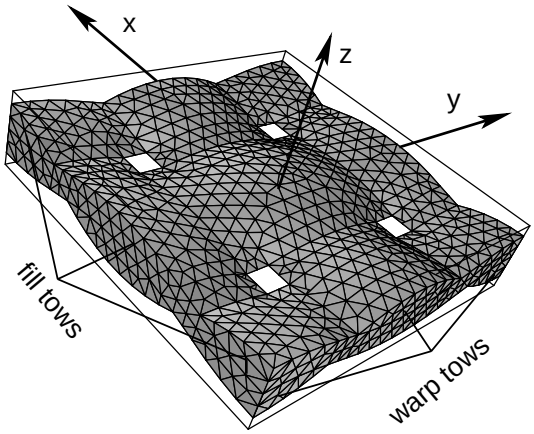

Fig. A.1. Schematic representation plain weave geometry

The profile of the warp tow centroid p_c is described by the relation

$$p_c(x) = -\sin\left(\frac{\pi x}{a}\right), \tag{A.1}$$

while the profile of the fill tow centroid follows from the previous relation by an appropriate change of x and y coordinates and the sign (see Eq. (A.8)). To maintain compatibility between warp and fill tows, the internal profiles of tows p_i are provided by

$$p_i(x) = \sin\left(\frac{\pi|x|}{a}\right). \tag{A.2}$$

The external profile p_e is derived from analogous relation with amplitude modified to take into account the non-symmetry of tows and the presence of the gap between tows g,

$$p_e(x) = (1+\beta)\sin\left(\frac{\pi(|x| - g/2)}{a-g}\right) - \beta, \tag{A.3}$$

with the coefficient β defined as

$$\beta = \sin\left(\frac{\pi g}{2a}\right). \tag{A.4}$$

The auxiliary functions R, F_H and F_R are used to linearly interpolate these one dimensional functions in order to obtain representation of lower and upper surfaces of individual tows,

$$F_H(x) = H\left(|x| - \frac{g}{2}\right) - H\left(|x| + \frac{g}{2} - a\right), \tag{A.5}$$

$$R(x) = \begin{cases} x/g + 1/2, & |x| \le g/2, \\ H(x), & g/2 < |x| \le a - g/2, \\ (\operatorname{sgn}(x)a - x)/g + 1/2, & a - g/2 < |x| \le a, \end{cases} \tag{A.6}$$

$$F_R(\eta, x, y) = R(\eta \operatorname{sgn}(y)x), \tag{A.7}$$

where H stands for the Heaviside function, sgn denotes the signum function and parameter $\eta = 1$ is used for the upper surface of a tow while $\eta = -1$ corresponds to the lower surface of a tow. Finally, the warp and fill tow surfaces are determined by

$$s_{\text{warp}}(\eta, x, y) = s_{\text{tow}}(\eta, x, y),\ s_{\text{fill}}(\eta, x, y) = -s_{\text{tow}}(-\eta, y, x), \tag{A.8}$$

where the general tow surface function $s_{\text{tow}}(\eta, x, y)$ for positions $|x| \le a$ and $|y| \le a$ is defined as

$$s_{\text{tow}}(\eta, x, y) = \frac{b}{2} F_H(y) \left(\operatorname{sgn}(y) p_c(x) + \eta F_R(\eta, x, y) p_i(y) + \eta F_R(-\eta, x, y) p_e(y)\right). \tag{A.9}$$

Finally, the orientation of fibers within the tows is assumed to be parallel to the centroid axes of the tows; the corresponding angles of rotation are given by

$$\theta_y^{\text{warp}}(x, y) = \arctan\left(-\frac{\pi b}{2a} \operatorname{sgn}(y) \cos(\frac{\pi x}{a})\right), \tag{A.10}$$

$$\theta_x^{\text{fill}}(x, y) = \arctan\left(-\frac{\pi b}{2a} \operatorname{sgn}(x) \cos(\frac{\pi y}{a})\right). \tag{A.11}$$